

Vibrational modes of nanolines*

Paul R Heyliger¹, Colm M Flannery² and Ward L Johnson²

¹ Department of Civil and Environmental Engineering, Colorado State University, Fort Collins, CO 80525, USA

² Materials Reliability Division, National Institute of Standards and Technology, 325 Broadway, Boulder, CO 80305, USA

E-mail: prh@engr.colostate.edu

Received 7 September 2007, in final form 21 January 2008

Published 5 March 2008

Online at stacks.iop.org/Nano/19/145707

Abstract

Brillouin-light-scattering spectra previously have been shown to provide information on acoustic modes of polymeric lines fabricated by nanoimprint lithography. Finite-element methods for modeling such modes are presented here. These methods provide a theoretical framework for determining elastic constants and dimensions of nanolines from measured spectra in the low gigahertz range. To make the calculations feasible for future incorporation in inversion algorithms, two approximations of the boundary conditions are employed in the calculations: the rigidity of the nanoline/substrate interface and sinusoidal variation of displacements along the nanoline length. The accuracy of these approximations is evaluated as a function of wavenumber and frequency. The great advantage of finite-element methods over other methods previously employed for nanolines is the ability to model any cross-sectional geometry. Dispersion curves and displacement patterns are calculated for modes of polymethyl methacrylate nanolines with cross-sectional dimensions of 65 nm × 140 nm and rectangular or semicircular tops. The vibrational displacements and dispersion curves are qualitatively similar for the two geometries and include a series of flexural, Rayleigh-like, and Sezawa-like modes.

1. Introduction

Nanoimprint lithography is a candidate for fabricating patterned polymers with length scales beyond the fundamental limits of conventional photolithography. However, the production of reliable high-quality patterns with nanoimprint lithography faces a number of obstacles relating to the mechanics of imprinting, cooling from the imprinting temperature, and removal of the mold [1]. Successful optimization of these processes requires knowledge of elastic stiffnesses and viscosity, which are expected to deviate significantly from bulk values as dimensions approach those of the molecular chains (typically, tens of nanometers) [2, 3]. No experimental methods have been established for providing quantitative information on these properties. In this report, we formulate and evaluate finite-element (FE) methods for modeling the vibrational modes of polymeric nanolines on substrates and present calculations of modes in nanolines with two different cross-sectional geometries. This work provides a theoretical foundation for extracting elastic stiffnesses from Brillouin-light-scattering measurements.

Hartschuh *et al* [4] first demonstrated that vibrational modes in polymeric nanolines can be detected in Brillouin light scattering (BLS) and suggested that such measurements could provide a means of determining the elastic constants. In subsequent work [5], the form of the strain fields of the three lowest-frequency modes of these specimens was determined through comparison of the measured dispersion curves with FE calculations and calculations based on the methods of Farnell and Adler [6]. The lowest mode was found to be similar to the lowest-order Lamb wave of a nanoline of infinite height, having flexural displacements primarily parallel to the substrate and perpendicular to the long axis of the nanolines. The second and third modes were found to be similar to the Rayleigh and lowest Sezawa modes of an infinite film on a substrate ('blanket' film), which have displacements in the plane of the surface normal and wavevector (for elastically isotropic materials) that decrease with depth into the substrate [7]. In both of the publications by Hartschuh *et al*, photolithographically patterned, rather than imprinted, nanolines were used, and interpretation of the data was complicated by the presence of an antireflective coating with unknown elastic properties.

* This paper is a contribution of the National Institute of Standards and Technology and is not subject to copyright in the United States.

Inversion analysis of BLS spectra from imprinted polymethyl methacrylate (PMMA) nanolines was pursued by Johnson *et al* [8] using Farnell–Adler models, including an approximate correction for the effect of finite nanoline height on the flexural frequencies. The elastic constants and nanoline dimensions determined from this analysis were found to be physically unrealistic, presumably because of inaccuracies arising from the approximation of a blanket film in the models for the Rayleigh-like and Sezawa-like modes.

In neither the work of Hartschuh *et al* [5] nor that of Johnson *et al* [8] were the employed FE or Farnell–Adler methods described in any detail. The nonrectangular geometry of the actual nanolines and the domain of validity of approximations incorporated in the calculations were not considered. The significant problem of impractical computation times, with three-dimensional FE mesh spacings that achieve sufficient accuracy, also was not addressed.

To place the present work in perspective, it also is useful to note previous theoretical work on guided acoustic waves in ridges on substrates, which was motivated by potential application in acoustic circuit devices. Since exact calculation of dispersion curves and displacement patterns of the modes in such structures is intractable, various approximations have been employed. Oliner [9] developed a method based on microwave network theory for calculating acoustic modes in rectangular waveguides on substrates. This method was pursued in a number of subsequent publications, including those of Oliner *et al* [10, 11], Li *et al* [12], and Yen and Oliner [13]. Tu and Farnell [14] used a variational technique with polynomial-series approximation functions to calculate modes in rectangular waveguides on substrates.

The network theory and variational approaches have been limited to rectangular waveguides. More complex geometries, including trapezoidal and triangular cross sections, have been modeled with FE methods by Burrige and Sabina [15], Mason *et al* [16, 17], Lagasse *et al* [18–22], and others using the approximation of a truncated substrate. These FE studies focused on topological waveguides (surface ridges in homogeneous material) with a principle focus on the lowest-frequency flexural modes.

Interest in wave propagation in ridges declined rapidly after the 1970s because of the high dispersion of flexural modes and the difficulties of fabrication and transduction compared to surface-acoustic-wave (SAW) devices. A review of work on this subject through 1976 is presented by Oliner [11].

The flexibility of FE methods with respect to the cross-sectional geometry has led to these methods being the primary focus of the present report. However, to estimate the range of validity of approximations in the FE calculations, Farnell–Adler methods also are employed here, and these are described in the following section. Section 3 describes the basic variational approach of the FE method and, then, considers approximations in the boundary conditions and the convergence as a function of mesh size. The problem of great computation time with full three-dimensional FE meshes is addressed through the approximation of sinusoidal variation of displacements along the length of a nanoline. In section 4, results are presented for a nanoline with a rectangular cross section and a nanoline with a semicircular top.

2. Farnell–Adler models

2.1. General method

Since the Farnell–Adler method for calculating elastic wave propagation characteristics in layered materials has been well described by Farnell and Adler [6], only a brief summary of this method is presented here. For an anisotropic plate or layer, the particle displacements are assumed to be linear combinations of partial waves having the form

$$u_j = \alpha_j \exp(ikby) \exp[i(kz - \omega t)], \quad (1)$$

where t is time, \hat{z} is parallel to the surface, \hat{y} is perpendicular to the surface, the subscript j refers to the three Cartesian coordinate axes, the α_j are constants determining the relative amplitudes of the components, and b is a complex quantity determining the oscillations and decay with depth.

The three equations of motion,

$$\rho \frac{\partial^2 u_j}{\partial t^2} = C_{ijkl} \frac{\partial^2 u_j}{\partial x_i \partial x_l}, \quad (2)$$

must be satisfied, where ρ is density and the C_{ijkl} are components of the elastic stiffness tensor. The boundary conditions also must be satisfied. At a free surface, the three components of traction stress must be zero. At an interface, the particle displacements and traction stresses must be continuous across the boundary. For a free plate, this results in six boundary conditions, and, for a layer on an infinite substrate, nine boundary conditions. These conditions, combined with the equations of motion, lead to a set of simultaneous equations that determines the normal modes. The determinant of the matrix of coefficients can be solved numerically to determine the eigenvalues (ω) and eigenvectors (displacements given by the α_j) of each of the modes.

The determinant is 6×6 for a plate and 9×9 for a layer on substrate. However, when the wave propagates along a crystal axis, the surface-wave components are purely sagittal (having no displacements perpendicular to the surface normal and propagation direction), making the determinant 4×4 for plates and 6×6 for a layer on a substrate.

2.2. Application to nanolines

Hartschuh *et al* [5] and Johnson *et al* [8] presented Farnell–Adler calculations for Rayleigh-like and Sezawa-like modes that neglect the finite widths of nanolines, approximating them as blanket films with a thickness equal to the height of the nanolines. Despite the crudeness of this approximation, the frequencies from such calculations were found by these authors to be fairly close to frequencies measured with BLS, at least for the geometries considered, and the correspondence with measurements provided insight into the general form of the strain fields of the modes.

The reason for the relative success of the Farnell–Adler calculations is that the dependence of strain on position over the width of these nanolines is not great for the Rayleigh-like and lowest-order Sezawa-like modes of nanolines. In other words, the displacements are primarily in the vertical

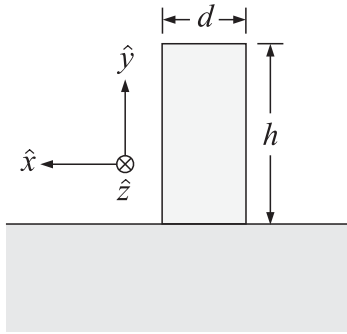


Figure 1. Schematic cross-sectional view of a nanoline on a semi-infinite substrate, including definitions of coordinate axes and dimensional parameters. The nanoline is assumed to be infinite in length along \hat{z} .

plane defined by the substrate normal and the axis lying along the length of the nanolines (as they are for true Rayleigh and Sezawa modes), and this has been illustrated in FE calculations [8]. In the present study, the approximation of a blanket film is employed in Farnell–Adler calculations.

In contrast to this situation with Rayleigh-like and Sezawa-like modes, the flexural modes have large transverse components, so that the approximations employed in Farnell–Adler calculations of these modes must be entirely different. To predict the dispersion curves of these modes, Hartschuh *et al* [5] employed the approximation of infinite nanoline extent perpendicular to the substrate, which leads to the dispersion curves of Lamb waves of a plate. Johnson *et al* [8] introduced finite height into the flexural mode calculations using a transverse resonance correction to the Lamb-wave calculations. This method is employed here. The flexural modes are approximated as Lamb waves in plates with a thickness equal to the nanoline width (thickness in the \hat{x} direction, as defined in figure 1), with the effect of y -dependence of displacements included by adjusting the wavenumbers in the dispersion curves according to the transverse-wave approximation of Li *et al* [12]:

$$(k_p^2 - k^2)^{\frac{1}{2}} = \frac{k_p^2}{k_s^2} (k_p^2 - k_s^2)^{\frac{1}{2}} \cot[(k_p^2 - k^2)^{\frac{1}{2}} h]. \quad (3)$$

In this equation, h is the height of the ridge and k , k_p and k_s are, respectively, the wave numbers (2π /wavelength) of the guided mode, the lowest Lamb plate mode, and the shear mode in the bulk.

3. Finite-element models

3.1. Variational formulation

The starting point for the FE model is Hamilton’s principle for the normal vibrational modes of an elastic medium:

$$0 = \delta \int_{t_0}^t dt \int_V [\frac{1}{2} \rho \dot{u}_j \dot{u}_j - U(S_{kl})] dV + \int_{t_0}^t dt \int_S T_k \delta u_k dS, \quad (4)$$

where V and S are the volume and surface occupied by and bounding the solid, T is the specified surface traction, δ is the variational operator, superscripts ‘.’ represent differentiation with respect to time, subscripts j and k refer to the three Cartesian coordinate axes, and U is the strain energy density. This latter quantity simplifies for linear elastic solids to a quadratic function of the infinitesimal strains S_{ij} as

$$U = \frac{1}{2} C_{ijkl} S_{ij} S_{kl}. \quad (5)$$

The weak form of the governing equations, as well as the governing differential equations themselves, can be found by applying the variational operator in equation (4) over a typical element. Substituting equation (5) into (4) and performing the required operations yield the final weak form, which provides the basis for numerical approximation. It is possible to integrate this expression by parts to give the three equations of motion. For brevity, results of this step are not included here.

For a given nanoline geometry, approximate solutions for the three displacement components are sought in the form of finite linear combinations of unknown constants multiplying predetermined approximation functions. In FE models, these constants take the form of the nodal displacements, and the approximation functions have the form

$$u(x, y, z, t) = \sum_{p=1}^n U_p(t) \Psi_p^u(x, y, z) \quad (6a)$$

$$v(x, y, z, t) = \sum_{p=1}^n V_p(t) \Psi_p^v(x, y, z) \quad (6b)$$

$$w(x, y, z, t) = \sum_{p=1}^n W_p(t) \Psi_p^w(x, y, z), \quad (6c)$$

where the displacements u , v , and w are in the \hat{x} , \hat{y} , and \hat{z} directions, respectively. The Ψ_p are typical three-dimensional shape functions used for general solid elements. The variations in the displacement variables are taken to be the approximation functions applied sequentially over an element. These functions can be chosen to have a variety of different forms (see Zienkiewicz and Taylor [23], for example), depending on the geometry and the order of approximation used for each variable. In our study, eight-noded brick elements with full integration are used for rectangular nanolines. We omit further details of this approach.

The spatially independent functions $U_p(t)$, $V_p(t)$, and $W_p(t)$ are associated with the individual subscript p and correspond to independent shape functions, as denoted by Ψ_p^u , Ψ_p^v , and Ψ_p^w , respectively. The superscripts on the functions indicate that the approximation functions for each of the variables need not be the same. Although solutions can be determined for the general transient case, the focus in this study is on the calculation for continuous periodic motion with angular frequency ω . Hence, we assume

$$U_p(t) = U_p \sin \omega t \quad (7a)$$

$$V_p(t) = V_p \sin \omega t \quad (7b)$$

$$W_p(t) = W_p \sin \omega t. \quad (7c)$$

Substitution of equations (6) and (7) and collection of terms enable the weak form from Hamilton's principle to be expressed in matrix form as

$$\begin{aligned}
 & -\omega^2 \begin{bmatrix} [M^{11}] & [0] & [0] \\ [0] & [M^{22}] & [0] \\ [0] & [0] & [M^{33}] \end{bmatrix} \begin{Bmatrix} \{U\} \\ \{V\} \\ \{W\} \end{Bmatrix} \\
 & + \begin{bmatrix} [K^{11}] & [K^{12}] & [K^{13}] \\ [K^{21}] & [K^{22}] & [K^{23}] \\ [K^{31}] & [K^{32}] & [K^{33}] \end{bmatrix} \begin{Bmatrix} \{U\} \\ \{V\} \\ \{W\} \end{Bmatrix} \\
 & = \begin{Bmatrix} \{F^1\} \\ \{F^2\} \\ \{F^3\} \end{Bmatrix}. \quad (8)
 \end{aligned}$$

This expression is valid for every element in the mesh, with the square of the frequency representing the eigenvalue. When the element equations are assembled into the final global matrix, the integrated tractions represented in the right-hand-side vector will all vanish from inter-element traction continuity, and the displacement vectors containing the elements of U , V , and W represent the global eigenvectors that correspond to the deformed shape of the mesh for a given eigenvalue. In general, the procedure for solving equation (8) implies fixing the geometry, boundary conditions, density, and elastic constants of the object for which solutions are sought. A standard eigensolver can then be employed to determine the eigenvalues (ω) and corresponding eigenvectors (displacement patterns).

3.2. Boundary conditions

Any formulation of an FE model for nanolines is confronted with two significant obstacles associated with boundary conditions and the size of the domain in which a solution is sought. First, even though acoustic waves are expected to be guided by the nanolines, the displacements of these guided waves also are expected to have finite amplitudes in the substrate, decreasing with depth in the same manner as surface waves of thin films. A finite substrate can be included in an FE calculation, but this will introduce resonant artifacts that complicate interpretation of the results. The second size-related obstacle arises from the fact that nanolines have cross-sectional dimensions that are orders of magnitude smaller than the length. In published BLS studies of nanolines [4, 5, 8], cross-sectional dimensions were as small as 65 nm, and lengths were $\sim 10 \mu\text{m}$. The detected acoustic modes had characteristic wavelengths on the order of 0.27–1.0 μm along \hat{z} and tens of nanometers over the cross section. Even for the lowest-frequency modes, a complete FE analysis of such measurements requires a three-dimensional mesh with spacings at least as small as a few nanometers over the cross section and a few tens of nanometers along the length. With the mesh extending over a length of 10 μm , the FE computation time is impractical. To deal with the computational difficulty of the problem, alternate approximate boundary conditions at the nanoline/substrate interface and the ends of the nanolines are considered in this section.

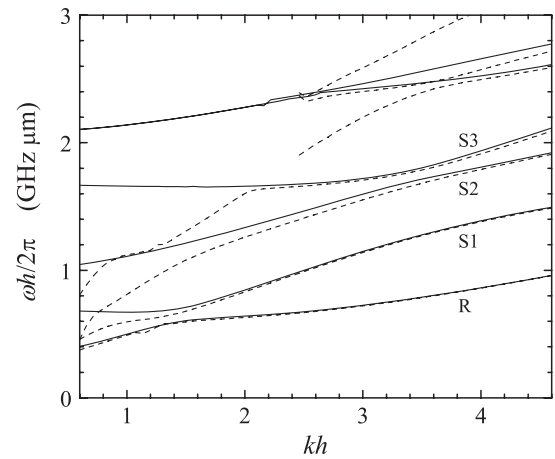


Figure 2. Farnell–Adler calculations of $\omega h/2\pi$ versus kh showing the effect of introducing rigidity of the nanoline/substrate interface. Solid lines: rigid interface. Dashed lines: nonrigid interface. The Rayleigh mode is labeled R. The first, second, and third Sezawa modes are labeled S1, S2, and S3. Higher unlabeled curves are also Sezawa modes.

3.2.1. Nanoline/substrate interface. Since silicon is much stiffer than polymers, one can consider approximating the displacements of guided waves in polymeric nanolines as zero at the interface, at least over a limited range of wave numbers. To estimate the uncertainty introduced by such an approximation into calculated nanoline guided-wave frequencies for a typical polymer, Farnell–Adler calculations were performed of Rayleigh and Sezawa modes of a blanket film of PMMA both with and without a fixed interface. The assumption in this analysis is that the corresponding modes in nanolines have a similar dependence of the vibrational amplitudes on y .

To provide input parameters for numerical modeling, BLS measurements of bulk longitudinal and shear waves were performed on a plate of PMMA with a thickness of approximately 17 μm , and density measurements were performed on a larger piece of PMMA. From these measurements, the longitudinal and shear velocities were determined to be 2778 and 1336 m s^{-1} (assuming a value of 1.493 [24] for the index of refraction) and the density was determined to be 1187 kg m^{-3} . These values correspond to elastic moduli $C_{11} = 9.161 \text{ GPa}$ and $C_{44} = 2.119 \text{ GPa}$. The film thickness was chosen to be 140 nm, which is comparable to the heights of nanolines studied with BLS.

Results of Farnell–Adler calculations with these parameters are shown in figure 2 for the Rayleigh mode and several Sezawa modes in the range of normalized wavenumbers kh from 0.6 to 4.6, which spans the typical range of k in BLS measurements with h in the range of 50–200 nm. Over the plotted range, the Rayleigh mode (R) frequency is affected relatively little by fixing the interface, the two calculations differing by less than 1.8% above $kh = 1.0$. For the first and third Sezawa modes (S1 and S3), the rigid-interface approximation has a more limited range of validity; agreement with the nonrigid calculations is achieved within 1.8% above $kh = 2.0$ and $kh = 2.1$, respectively. For the second Sezawa mode (S2), this

level of agreement is achieved only above $kh = 3.6$. With respect to application in inversion analysis of dispersion curves measured with BLS, figure 2 shows that the interface can be accurately approximated as rigid if the inversion is limited to these respective ranges of kh for each curve.

The flexural modes are not included in figure 2, because the introduction of rigidity of the interface in the Farnell–Adler calculations for these modes is less straightforward. The accuracy of the calculations for the lowest flexural mode is briefly considered in section 4 when comparing Farnell–Adler and FE results.

3.2.2. End surfaces. The surfaces at the ends of a nanoline (perpendicular to \hat{z}) are traction-free. This leads to modal displacement patterns at and near the ends that differ from the typical character away from the ends. As the length of the nanoline increases, these effects have less influence on the frequencies of the modes, since the elastic and kinetic energies away from the ends more strongly determine the frequency and the variation along \hat{z} is more closely approximated as spatially harmonic (the Fourier transform of the z dependence is approximately a delta function).

To explore the influence of the traction-free ends, two separate FE models were constructed. The first was fully three-dimensional (3D), employing conventional shape functions that can represent the displacements in a finite nanoline. In the second model, the three displacement components were approximated as varying with fixed harmonic dependence in z , leading to a semi-analytic formulation in which the z -dependence of the displacements is eliminated but the wavenumber k along \hat{z} appears as an input parameter. This model dramatically reduces computational time, but introduces wavelength-dependent errors in the calculated dispersion curves. It provides the full displacement pattern from an FE calculation over a single cross-sectional plane for a given k and, therefore, is referred to here as two-dimensional (2D).

In the 2D approximation, the shape functions assume the form

$$u(x, y, z, t) = \sum_{p=1}^n U_j(t) \Psi_p^u(x, y) \sin kz \quad (9a)$$

$$v(x, y, z, t) = \sum_{p=1}^n V_j(t) \Psi_p^v(x, y) \sin kz \quad (9b)$$

$$w(x, y, z, t) = \sum_{p=1}^n W_j(t) \Psi_p^w(x, y) \cos kz. \quad (9c)$$

The relative phases of the z -dependence of the three displacement components are based on the facts that (1) the components correspond to these harmonic functions in the case of fully three-dimensional modeling, and (2) this is the required dependence of these displacement components on z when they are directly substituted into the three-dimensional differential equations of motion.

The variations of the primary field variables are then taken as

$$\delta u = \Psi_p^u(x, y) \quad (10a)$$

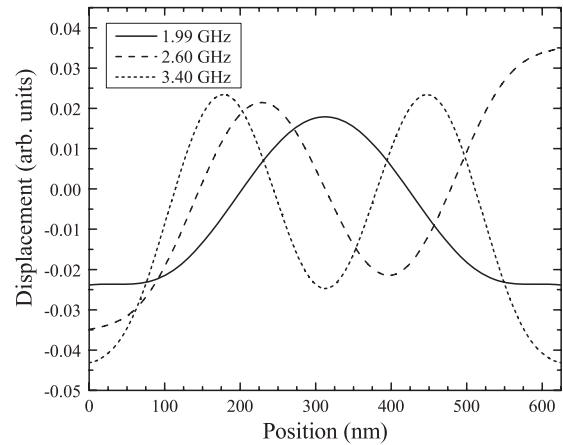


Figure 3. Amplitudes of x -displacements of the three lowest-frequency modes as a function of z at an upper corner of a nanoline. The frequencies of the three modes are listed in the legend. The nanoline length is 625 nm, d is 65 nm, and h is 140 nm.

$$\delta v = \Psi_p^v(x, y) \quad (10b)$$

$$\delta w = \Psi_p^w(x, y). \quad (10c)$$

The elements of the coefficient matrices in equation (8) under the approximation of equation (9) are given in the appendix. The corresponding matrix expressions for the 3D model are not given here but can be found elsewhere [25].

To evaluate the accuracy of the approximation of sinusoidal z dependence, 3D FE calculations of resonant frequencies of finite nanolines were compared with 2D FE calculations of dispersion curves (frequency versus wavenumber). While k is a continuously adjustable input parameter in the 2D formulation, it is determined entirely by the resonant standing-wave patterns along the length in the 3D formulation. Therefore, the 3D calculations yield only discrete points on dispersion curves.

A representative rectangular PMMA nanoline was considered with a width d of 65 nm and a height h of 140 nm. In order to keep computation times at a practical level, the length was taken to be 625 nm, more than an order of magnitude smaller than nanolines that have been studied with BLS. The nanoline/substrate interface was fixed. In both the 3D and 2D formulations, nanoline cross sections were discretized into two volume elements (three grid points) in the \hat{x} direction and four volume elements in the \hat{y} direction. This cross-sectional mesh is a very coarse discretization of the nanoline, and the frequencies will not match those of more detailed representations; the goal of this analysis was only to determine the level of accuracy of the 2D approximation relative to the 3D calculation. Two different discretizations along \hat{z} were employed: 60 elements and 120 elements.

Figure 3 shows, for the three lowest-frequency modes, 3D calculations of displacements in the \hat{x} direction as a function of z at an upper corner of the nanoline with 120 mesh elements along \hat{z} . All of these modes are predominantly flexural. Similar calculations with 60 elements along \hat{z} are essentially indistinguishable, on the scale of figure 3, from those shown, indicating that the number of elements in this

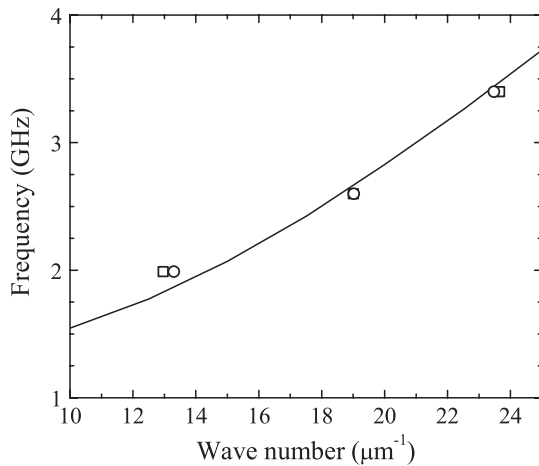


Figure 4. Dispersion curve computed with the 2D model (solid line) and discrete points computed with the 3D model for a nanoline with a length of 625 nm, $d = 65$ nm, and $h = 140$ nm. Wave numbers for the 3D calculation were determined by fitting the displacement patterns (figure 3) to a sine function plus a constant, with points within 100 nm (circles) or 50 nm (squares) of the ends excluded.

direction is sufficient to accurately represent the z -dependence. The traction-free surfaces at $z = 0$ and 625 nm destroy the otherwise approximately harmonic nature of the modal displacement pattern over distances on the order of 100 nm near the ends.

Figure 4 shows values of frequency versus approximate wavenumber from the above calculation with 120 elements along z . The values of wavenumber were obtained by least-squares fitting of the displacement patterns of figure 3 to a sine function plus a constant, excluding points within 100 or 50 nm of the ends of the nanoline. The solid curve was obtained from the 2D model. With the exception of the lowest-frequency 3D mode, the 3D and 2D calculations are in close agreement; they differ by $\sim 1\%$ for the highest mode with points excluded within 100 nm of the ends. These results indicate that the 2D model can provide accurate dispersion curves of modes with wavelengths (away from the ends) that are less than half the length of the nanoline. For the polymeric nanolines in published experimental BLS studies, this certainly was the case. The nanolines studied with BLS by Hartschuh *et al* [5] and Johnson *et al* [8] were 10 μm in length, an order of magnitude greater than the shortest wavelengths of the measured acoustic modes and two orders of magnitude greater than the length of the regions where end effects are seen to be significant in figure 3.

3.3. Convergence

The analyses above indicate that the approximations of a rigid nanoline/substrate interface and sinusoidal z dependence introduce little error in the dispersion curves calculated with the FE methods, at least for the modes and ranges of wavenumbers discussed in section 3.2.1. Both of these approximations are employed in the remainder of this report.

The accuracy of FE calculations also depends on the selected mesh size, with the calculated frequencies converging

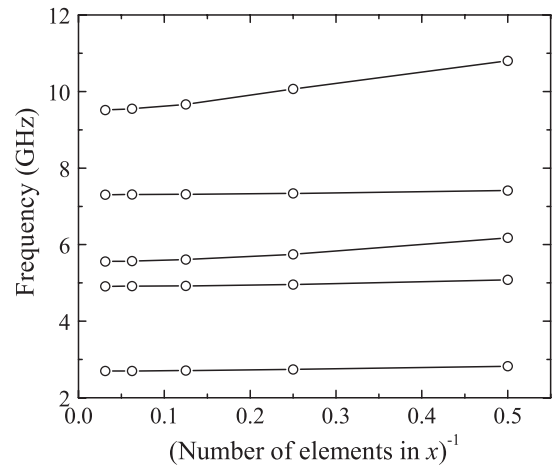


Figure 5. Calculated frequencies in the 2D model as a function of the inverse of the number of mesh elements in the cross section.

to true values from above as the mesh is made finer. A convergence study was performed to determine the level of discretization necessary to obtain good results for at least the lowest few modes with a typical wavenumber, $20 \mu\text{m}^{-1}$, in the measurable BLS range and typical cross-sectional dimensions of $d = 65$ nm and $h = 140$ nm. Conventional four-noded isoparametric finite elements were used to represent the rectangular domain of the nanoline cross section. The number of divisions in the \hat{x} direction was used to quantify the level of discretization of the mesh, with the number of elements in the \hat{y} direction twice that in the \hat{x} direction. Four cross-sectional discretizations were used: 2×4 , 4×8 , 8×16 , 16×32 , and 32×64 .

The results are summarized in figure 5, with the frequencies of the lowest five modes plotted against the inverse of the number of elements in the \hat{x} direction. Hence, the mesh is refined on moving to the left in the plot, with the intercept on the vertical axis yielding a value closest to the exact frequency (within the rigid-interface and 2D approximations that are employed). The decrease in calculated frequency that results from a refining of the mesh from 8×16 to 16×32 , is 0.3%, 0.2%, 0.7%, and 0.1% for the first through fourth modes, respectively. The fifth mode also converges rapidly but slightly less so, with calculations for the 8×16 and 16×32 meshes differing by 1.2%. This behavior is expected for calculations employing Ritz-based finite-element models, with the weaker spatial dependence of displacements of the lower modes being easier to represent using a limited number of terms in the approximation functions. The calculations in figure 5 indicate that, if an accuracy for the frequencies on the order of 1% is desired, this can be achieved for the plotted modes by using a mesh of 8×16 .

4. Results

In this section, FE calculations of representative displacement patterns and dispersion curves are presented for PMMA nanolines with two cross-sectional geometries: the rectangular cross section discussed in the previous section and a rectangle

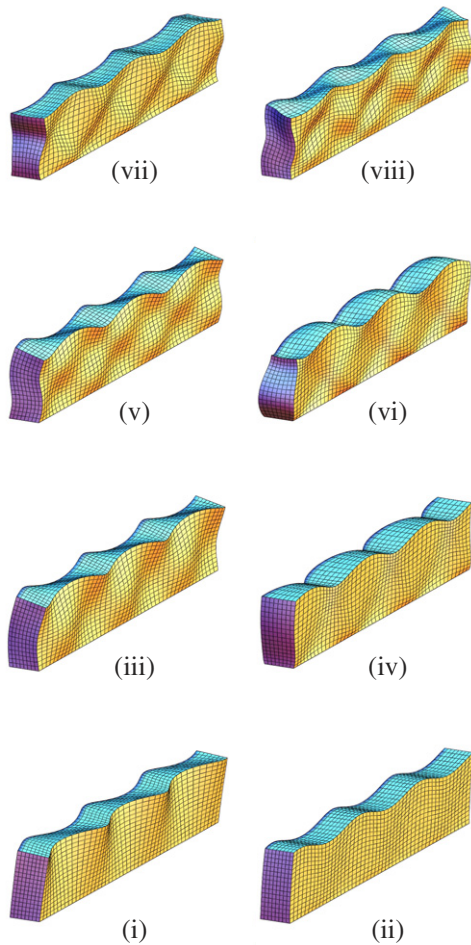


Figure 6. Calculated displacement patterns for the eight lowest-frequency modes with $k = 20 \mu\text{m}^{-1}$ in a rectangular nanoline with cross-sectional dimensions of $65 \text{ nm} \times 140 \text{ nm}$. The frequencies increase in the order of the mode labeling from (i) to (viii).

(This figure is in colour only in the electronic version)

region topped with a semicircular region. In both cases, d is taken to be 65 nm and the total height h is taken to be 140 nm . A mesh of 8×16 elements is used for the nanolines with a rectangular cross section. For the nanolines with semicircular tops, a 8×16 mesh is used for the rectangular region, and an additional 32 elements (8 circumferential divisions and 4 radial divisions) are used to represent the semicircular region. Since the total heights are the same for the two geometries, the cross-sectional area with the semicircular top is 5% lower than that with the rectangular geometry. Therefore, the semicircular model has a corresponding reduction in mass and stiffness, which affects the frequencies of the modes but not the general form of the displacements, as discussed below.

4.1. Rectangular cross section

Figure 6 shows FE calculations of displacement patterns in rectangular nanolines for modes below 12 GHz with $k = 20 \mu\text{m}^{-1}$. The first, third, fifth, and eighth modes have a flexural character, with displacements that are antisymmetric with respect to the vertical midplane extending along the

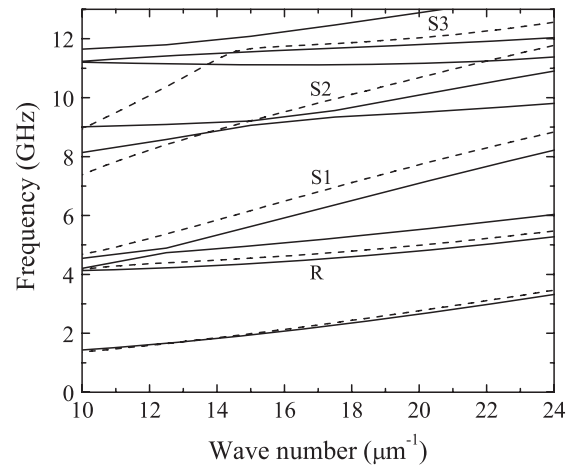


Figure 7. Solid lines: FE calculations for a nanoline with a rectangular cross section, $h = 140 \text{ nm}$, and $d = 65 \text{ nm}$. Dashed lines: Farnell-Adler calculations for the same geometry with the nanoline/substrate interface not rigid.

length (yz plane). The second, fourth, sixth, and seventh modes have displacements that are symmetric with respect to this midplane. For both types of modes, there is greater vertical phase variation at higher frequencies. The second and third modes have displacements similar to Rayleigh and lowest Sezawa modes of a blanket film, as previously reported [5, 8]. The higher-frequency symmetric modes have displacements similar to higher-order Sezawa modes, but with significant transverse (\hat{x}) components of the displacements. Note that these transverse components, which arise from the dynamic Poisson effect, have a different symmetry from flexural displacements, since they are symmetric with respect to the vertical midplane.

Figure 7 presents frequencies calculated with the FE model for modes below 13 GHz with wavenumbers in the range of $10\text{--}24 \mu\text{m}^{-1}$. The lowest eight frequencies at $20 \mu\text{m}^{-1}$ correspond to the modes plotted in figure 6. Farnell-Adler calculations of the dispersion curves (dashed lines) also are presented in this figure. As described above, these calculations employ the approximation of a blanket film for the Rayleigh-like and Sezawa-like modes and employ a transverse resonance correction to Lamb-wave frequencies for the lowest-frequency flexural mode. Higher-order flexural modes are not included in the Farnell-Adler calculations. The general correspondence of the Farnell-Adler calculations with the FE calculations up to mode S2 is consistent with the symmetries of the displacements seen in the FE calculations of figure 6. However, there are substantial differences in the magnitudes of the frequencies obtained from the two models for the Sezawa-like modes. Based on the analysis of the accuracy of the FE model in section 3, almost all of these differences (and those for the Rayleigh-like mode) can be attributed to inaccuracies in the Farnell-Adler calculations. In other words, the approximation of infinite width of the nanoline in the Farnell-Adler calculations for the Rayleigh-like and Sezawa-like modes leads to significant inaccuracies. On the other hand, the close agreement of the FE and Farnell-Adler calculations

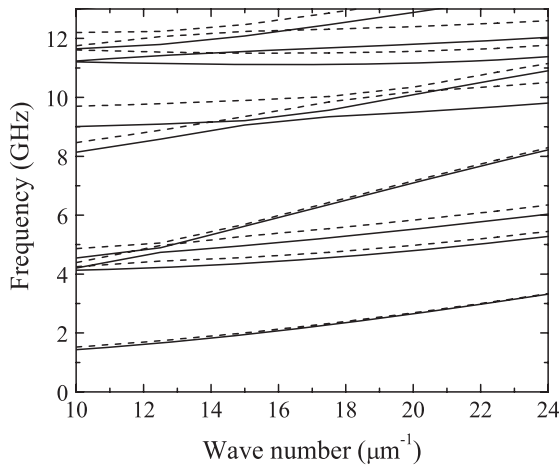


Figure 8. FE calculations of frequency versus wavenumber in nanolines with $h = 140$ nm and $d = 65$ nm. Dashed lines: semicircular top. Solid lines: rectangular top (as in figure 7).

for the lowest flexural mode suggests that the approximations involved in each of these approaches are quite accurate for this mode.

4.2. Cross section with semicircular top

When polymeric nanolines are imprinted, a thin layer of the polymer remains in the region between the nanolines. This residual layer is removed by etching, which introduces a rounding of the top surfaces of the nanolines. Therefore, for practical characterization of vibrational modes of polymeric nanolines, it is useful to include a rounded upper surface in the model geometry.

Calculated displacement patterns (not shown) for the nanoline with a semicircular upper surface are qualitatively similar to those for the nanoline with a rectangular cross section shown in figure 6. Results for the dispersion curves of a nanoline with this geometry are shown in figure 8 along with the results from figure 7 for the rectangular nanoline. Since the geometry with a semicircular top has 5% less volume than the rectangular geometry, the frequencies with the semicircular top are shifted upwards. The specific amount of this shift for each mode depends on the fraction of the acoustic energy that is present near the upper corners of the nanolines. Therefore, the relative spacings of the modes in figure 8 are affected by rounding of the top surface. Note, in particular, that the lowest flexural and Sezawa-like modes (the first and fourth curves from the bottom) are affected only slightly by rounding of the top, while the Rayleigh-like mode (second curve) is shifted more significantly upwards.

5. Conclusions

The FE methods presented here provide a flexible basis for modeling vibrational modes of polymeric nanolines on substrates. The great advantage of these methods relative to Farnell–Adler methods is that any finite cross-sectional geometry can be easily incorporated in the model. This

capability is essential for accurate modeling of vibrational modes in nanolines that are currently being fabricated, since the etching step in nanoimprint lithography typically leads to rounding of the tops and tapering of the sides of nanolines. Even in the case of rectangular cross sections, the approximation of a blanket film in the Farnell–Adler calculations for the Rayleigh-like and Sezawa-like modes is found here to introduce significant inaccuracies in the frequencies.

To make the FE calculations more practical in terms of computational time, the variations of displacements along the length have been approximated as sinusoidal with the wavenumber as an input parameter. Also, the nanoline/substrate interface has been approximated as rigid to simplify the analysis. These approximations have been found to be valid for the lowest flexural, Rayleigh-like, and lowest three Sezawa-like modes over limited ranges of wavenumbers.

Sample calculations on PMMA nanolines with rectangular and semicircular tops have shown similar series of flexural, Rayleigh-like, and Sezawa-like modes with differences in relative spacings of the dispersion curves. In a separate report [26], we will pursue the subject of inversion analysis of BLS data on imprinted PMMA nanolines using the methods that are presented here.

Acknowledgment

The authors thank Sudook Kim for providing measurements of elastic constants and density of PMMA.

Appendix. Elements of matrices

The elements of the coefficient matrices in equation (8) under the approximation of equation (9) are given by

$$K_{ij}^{11} = \int_V \left(C_{11} \frac{\partial \Phi_i^u}{\partial x} \frac{\partial \Phi_j^u}{\partial x} \cos^2 kz + C_{55} \Phi_i^u \Phi_j^u \sin^2 kz + C_{66} \frac{\partial \Phi_i^u}{\partial y} \frac{\partial \Phi_j^u}{\partial y} \cos^2 kz \right) dV \quad (\text{A.1})$$

$$K_{ij}^{12} = \int_V \left(C_{12} \frac{\partial \Phi_i^u}{\partial x} \frac{\partial \Phi_j^v}{\partial y} + C_{66} \frac{\partial \Phi_i^u}{\partial y} \frac{\partial \Phi_j^v}{\partial x} \right) \cos^2 kz dV = K_{ji}^{21} \quad (\text{A.2})$$

$$K_{ij}^{13} = \int_V \left(C_{13} \frac{\partial \Phi_i^u}{\partial x} \Phi_j^w k \cos^2 kz - C_{55} \Phi_i^u \frac{\partial \Phi_j^w}{\partial x} k \sin^2 kz \right) dV = K_{ji}^{31} \quad (\text{A.3})$$

$$K_{ij}^{22} = \int_V \left(C_{22} \frac{\partial \Phi_i^v}{\partial y} \frac{\partial \Phi_j^v}{\partial y} \cos^2 kz + C_{44} \Phi_i^v \Phi_j^v k^2 \sin^2 kz + C_{66} \frac{\partial \Phi_i^v}{\partial x} \frac{\partial \Phi_j^v}{\partial x} \cos^2 kz \right) dV \quad (\text{A.4})$$

$$K_{ij}^{23} = \int_V \left(C_{23} \frac{\partial \Phi_i^v}{\partial y} \Phi_j^w k \cos^2 kz - C_{44} \Phi_i^v \frac{\partial \Phi_j^w}{\partial y} k \sin^2 kz \right) dV = K_{ji}^{32} \quad (\text{A.5})$$

$$K_{ij}^{33} = \int_V \left(C_{33} \Phi_i^w \Phi_j^w k^2 \cos^2 kz + C_{44} \frac{\partial \Phi_i^w}{\partial y} \frac{\partial \Phi_j^w}{\partial y} \sin^2 kz + C_{55} \frac{\partial \Phi_i^w}{\partial x} \frac{\partial \Phi_j^w}{\partial x} \sin^2 kz \right) dV. \quad (\text{A.6})$$

$$M_{ij}^{11} = \int_V \rho \Phi_i^u \Phi_j^u \sin^2 kz dV \quad (\text{A.7})$$

$$M_{ij}^{22} = \int_V \rho \Phi_i^v \Phi_j^v \sin^2 kz dV \quad (\text{A.8})$$

$$M_{ij}^{33} = \int_V \rho \Phi_i^w \Phi_j^w \cos^2 kz dV. \quad (\text{A.9})$$

References

- [1] Guo L J 2004 *J. Phys. D: Appl. Phys.* **37** R123
- [2] Van Workum K and de Pablo J J 2003 *Nano Lett.* **3** 1405
- [3] Stafford C M, Vogt B D, Harrison C, Julthongpipit D and Huang R 2006 *Macromolecules* **39** 5095
- [4] Hartschuh R, Ding Y, Roh J H, Kisliuk A, Sokolov A P, Soles C L, Jones R L, Hu T J, Wu W L and Mahorowala A P 2004 *J. Polym. Sci. B* **42** 1106
- [5] Hartschuh R D, Kisliuk A, Novikov V, Sokolov A P, Heyliger P R, Flannery C M, Johnson W L, Soles C L and Wu W-L 2005 *Appl. Phys. Lett.* **87** 173121
- [6] Farnell G and Adler E 1972 *Physical Acoustics* vol 9, ed W P Mason and N Thurston (New York: Academic) p 35
- [7] Auld B A 1990 *Acoustic Fields and Waves in Solids* vol 2 (Malabar, FL: Krieger)
- [8] Johnson W L, Flannery C M, Kim S A, Geiss R, Heyliger P R, Soles C L, Hu W and Pang S W 2006 *Mater. Res. Soc. Symp. Proc.* **924** Z08-31
- [9] Oliner A A 1969 *IEEE Trans. Microw. Theory Tech.* **17** 812
- [10] Oliner A A, Bertoni H L and Li R C M 1972 *Proc. IEEE* **60** 1503
- [11] Oliner A A 1976 *Proc. IEEE* **64** 615
- [12] Li R C M, Bertoni H L, Oliner A A and Markham S 1972 *Electron. Lett.* **8** 211
- [13] Yen K H and Oliner A A 1976 *Appl. Phys. Lett.* **28** 368
- [14] Tu C C and Farnell G W 1973 *IEEE Trans. Sonics Ultrason.* **20** 302
- [15] Burrige R and Sabina F J 1971 *Electron. Lett.* **7** 720
- [16] Mason I M, De la Rue R M, Schmidt R V, Ash E A and Lagasse P E 1971 *Electron. Lett.* **7** 395
- [17] Mason I M, De La Rue R M, Lagasse P E, Schmidt R V and Ash E A 1972 *IEEE Trans. Sonics Ultrason.* **19** 394
- [18] Lagasse P L and Mason I M 1972 *Electron. Lett.* **8** 82
- [19] Lagasse P L 1972 *Electron. Lett.* **8** 372
- [20] Lagasse P L, Mason I M and Ash E A 1973 *IEEE Trans. Sonics Ultrason.* **20** 143
- [21] Lagasse P L 1973 *IEEE Trans. Sonics Ultrason.* **20** 354
- [22] Lagasse P L 1973 *J. Acoust. Soc. Am.* **53** 1116
- [23] Zienkiewicz O C and Taylor R L 1989 *The Finite Element Method* 4th edn, vol 1 (London: McGraw-Hill)
- [24] Prasciolu M, Candeloro P, Kumar R, Businaro L, Di Fabrizio E, Cojoc D, Cabrini S, Liberale C and Degiorgio V 2003 *Japan. J. Appl. Phys.* **42** 4177
- [25] Heyliger P R and Jilani A 1992 *Int. J. Solids Struct.* **29** 2689
- [26] Johnson W L et al 2008 in preparation